Region of Interest Image Reconstruction for Compton Imaging Using 3-D Position Sensing CdZnTe

Valerie E. Nwadeyi^{ID}, *Member, IEEE*, Jeffrey A. Fessler^{ID}, *Fellow, IEEE*, and Zhong He, *Senior Member, IEEE*

Abstract—**Iterative methods, such as list-mode maximum likelihood expectation maximization (LM-MLEM) provide high signal-to-noise ratio reconstructions for Compton imaging. However, MLEM reconstructions can be computationally expensive when reconstructing a high-resolution image over the full field of view (FOV). When employing MLEM for high-resolution imaging, a vast number of data pixels would be needed. This work proposes a region of interest MLEM algorithm (ROI-MLEM) for Compton imaging, using 3-D position sensing CdZnTe, that allows for image reconstruction to take place within a fixed ROI based on prior knowledge of the approximate location of the source. ROI-MLEM is demonstrated by reconstructing simulated and experimental ^{137}Cs source measurements. A preliminary study of the ROI-MLEM performance in high-energy imaging is shown by reconstructing the Compton image of the 4.44 MeV photopeak from a PuBe source. ROI-MLEM shows a 44% improvement in the signal-to-noise ratio (SNR) compared to standard MLEM for simulated source reconstructions in a truncated FOV. The experimental results show the capabilities of estimating the source location with submillimeter pixel resolution at a 30-cm source-to-detector distance, resulting in an average error of 1.4 mm in source location estimation.**

Index Terms—**Compton imaging, image reconstruction, list-mode (LM), maximum likelihood expectation maximization (MLEM), region of interest (ROI), truncated field of view (FOV).**

I. INTRODUCTION

COMPTON imaging uses multi-scatter events per photon to reconstruct the spatial distribution of a radioactive source in a 4π field of view (FOV) about a gamma-ray detector. Many imaging applications desire the ability to use Compton scattering events to precisely image photon sources in real-time. For example, imaging the 4.438 MeV prompt gamma-ray emission from carbon scatter, with millimeter accuracy, is sought after in proton radiotherapy for beam range verification [1], [2].

As the photons interact with the detector there are many processes that can hinder the accurate reconstruction of a Compton image. Partial energy deposition events, chance coincidence, and pair production events at high photon energies can all lead to poor event reconstruction, causing poorly reconstructed Compton cones that can add unwanted noise to the imaging space. List-mode maximum likelihood expectation maximization (LM-MLEM) is an iterative imaging algorithm that can reduce the effect of noise artifacts in the image space due to poor event reconstruction. However, in the presence of high-frequency noise, which is often seen with high-energy gamma-ray imaging, where the data are sparse and incomplete, the high-frequency noise artifacts can overpower the true source location estimate and dampen the intensity of the source profile in the imaging space, even when implementing MLEM.

When using MLEM as an approach to Compton imaging, a complete representation of the source distribution in the entire FOV of the detector is needed as photons can intercept the detector from all directions. When reconstructing all possible source locations about the detector, the MLEM algorithm will spend a large portion of its computation reconstructing space in the FOV that is unimportant, particularly when the source dimension is small compared to the FOV. Reconstructing data in the unused region of the FOV can require substantial computational effort for high-resolution localization of the source distribution, as many small imaging pixels are needed for the entire FOV. There are many imaging applications where the computational cost of the iterative imaging algorithm is reduced, allowing for improved pixel resolution, by defining a smaller region of interest (ROI) than the detection system's full FOV [3]–[6].

This work demonstrates the use of an iterative ROI reconstruction method, ROI-MLEM, in which only the backprojected Compton rings that intersect a desired region within the 4π space about the detector are reconstructed with a fine pixelated mesh grid. ROI-MLEM adapts the method of Ziegler *et al.* [7] in which a mask is applied to a 4π FOV to allow for reconstruction of the ROI alone. Our approach deviates from Ziegler's application in that the Poisson nature of Compton rings precludes subtraction of the unwanted image space, so consideration must be given to the derivation of ROI-MLEM for Poisson data.

Imaging within a ROI allows the method to focus on the events that reconstruct within the desired region, accelerating the algorithmic convergence. Using ROI-MLEM, the

computational expense of the iterative process will be reduced as the high-resolution needs depend only on the pixelation of the ROI and not the entire 4π FOV.

This article discusses the complications of using standard LM-MLEM for ROI or truncated FOV imaging and how ROI-MLEM corrects for the complications through its derivation. The ROI-MLEM algorithm is then applied to simulated data to compare 4π MLEM and ROI-MLEM. The application of ROI-MLEM for high-resolution imaging is shown using experimental ^{137}Cs and PuBe source data, also demonstrating the enhanced computational performance using this novel technique for Compton imaging of high-energy photon sources.

II. Truncated FVO Imaging Using MLEM

List-mode MLEM is a widely used iterative method with applications to many Compton imaging problems [8]–[10]. In the case of 3-D position sensing CdZnTe (CZT) detection systems, there is no restriction, collimation, or preference to the incident direction of the impinging gamma rays. Because CZT can record events from any direction, full 4π Compton cone reconstructions are projected back to a spherical imaging space about the detector for source distribution imaging.

For list-mode data, all interactions for each photon detected are recorded as a single event and are summed assuming full energy deposition for each event. All possible sequences of these multi-scatter interactions are used to reconstruct Compton cones that can point to different locations and vary in probability of estimating the true source location based on the probability of the sequence order of the interactions [11]. To reconstruct an image of the most likely estimate of the true source distribution, LM-MLEM uses the following update equation to iterate over all Compton cones created for all events:

$$f_j^{n+1} = \frac{f_j^n}{s_j} \sum_{i=1}^{I} \frac{t_{ij}}{\sum_{j'=1}^{J} t_{ij'} f_{j'}^n} \qquad (1)$$

where f_j^n is the nth iteration estimate of the source distribution over the image space that is divided into J pixels. The system matrix element, t_{ij}, defines the spatial probability based on the Compton cones reconstructed for each permutation of the sequence order of the recorded scatters for each event, i, where $i = 1, 2, \ldots, I$ in pixel j, where $j \in \{1, 2, \ldots, J\}$. The system matrix element, t_{ij}, is developed as the Compton equation is calculated based on the multiscatter interaction for each photon [8]. In an ideal case, each image pixel the Compton ring intersects will have a probability of one and all other pixels will equal zero in the image space. To account for detector uncertainty, each ring is Gaussian blurred for a gradual descent to zero for all pixels that do not correspond to the Compton ring location [11]. The probability of detecting a photon from the jth pixel is defined by the sensitivity, s_j, which is assumed to be uniform in this work. The imaging space for (1) is the 4π directional space.

4π imaging has proven to be very useful in unknown source localization and far-field imaging [12]–[14]. However, in cases, such as proton beam range verification, where submillimeter resolution is desired and the expected FOV is well defined given the source parameters, 4π imaging

can be computationally expensive. In these scenarios, the desired FOV is much smaller than the given 4π space but requires small pixel sizes to aid in achieving the resolution requirements.

Therefore, conventional MLEM spends much computational time reconstructing an image in space where the source is not expected to be seen. Reconstructing that imaging space only increases the size of the data system matrix when multiplying the total number of reconstructed Compton cones with the number of pixels required to achieve a high-resolution result over the entire imaging space. Other issues are the noise artifacts in the image space that arise due to mis-sequencing of the Compton scatter events, pair production events at photon energies above 1.022 MeV, partial energy deposition events, and charge sharing and chance coincidence events that can exceed the detectors timing resolution and dynamic range; all of which can lead to incorrectly reconstructed Compton cones that point to shift-variant noise in the 4π imaging space that do not correspond to the true location of the source [15]. Due to the pixelation of CZT and Doppler broadening of the scatter within the crystal volume, there will be uncertainty in the position and energy resolution of the Compton events, which translate to the uncertainty in the Compton ring reconstruction via Gaussian blurring.

Truncating the FOV to a desired region about the assumed source location could alleviate the convergence to high-frequency artifacts in the image space when reconstructing noisy projections and reduce the number of pixels needed to achieve the fine pixel resolution required. However, applying standard list-mode MLEM to reconstruct a space smaller than the original 4π sphere will lead to artifacts along the edges or in the corners of the new FOV. As the FOV reduces in size, corner, and edge artifacts become more prominent and diminish the reconstruction of the source distribution.

The corner artifacts are due to an improper weighting of the Compton ring in the truncated image space, as portions of the ring outside of the desired FOV are no longer calculated in the system matrix. The truncated system matrix is calculated for the same Compton rings used in 4π imaging, providing an estimate of the source intensity in the newly redefined image space. However, the redefined estimate incorrectly describes the probability of those events that reconstruct outside of the truncated FOV or partially intersects the smaller imaging frame. This phenomenon can be explained by first analyzing the forward projection of the list-mode MLEM equation.

A. Forward Projection Analysis

The forward projection contributes to the likelihood estimate of each Compton event

$$\sum_{j'=1}^{J} t_{ij'} f_{j'}^n. \qquad (2)$$

And is a summation of the estimated probability distribution of all the Compton rings reconstructed for each event in the system matrix, multiplied by the previous source distribution estimate. Any truncation of the FOV from 4π will alter the projection of each Compton ring in the smaller imaging space.

Thus, the value of each forward projection would change due to the change in the FOV. If the FOV is truncated, so will parts of the Compton ring that are not within the new image space. Such truncation of the FOV could lead to inaccurate estimates of the summed probabilities of each Compton ring reconstructed for each event. Truncation of the Compton ring, due to a smaller FOV, would cause the forward projection to deviate from the original summed probabilities over the image space in 4π as the summation is now over a smaller number of pixels. This deviation can lead to two possible limits as the forward projection is calculated for each event, *i,* over all pixels within the redefined image space

Limit 1: $\sum_{j'=1}^{J} t_{ij'} f_{j'}^{n} \gg 1$

Limit 2: $\sum_{j'=1}^{J} t_{ij'} f_{j'}^{n} \ll 1$.

Limit 1 occurs when the reconstructed Compton rings are truncated such that the most probable locations of the Compton ring are within majority of the pixels in the truncated FOV. This limit can also be approached for a ring that is very wide due to Gaussian blurring caused by a large uncertainty in the event energy deposition or sequencing. If multiple Compton rings are reconstructed for the same event based on the varying sequencing order of the scattering interactions, this could also cause the forward projection value to increase above one. Especially so, if the most probable locations of each ring are within the smaller FOV.

Limit 2 is often associated with Compton rings that reconstruct near the edges or in the outer perimeter of the truncated FOV. This limit is most likely approached when the trailing end of the Compton ring's Gaussian curve is the only portion reconstructed within the smaller imaging space. This outermost edge of the Compton ring is the least likely location that the photon could have originated from and very few pixels of the truncated space will reflect these lower probability estimates, depending on how far away the Compton ring is projected from the source's location or the truncated FOV. This leaves little information about the full probability of the event for LM-MLEM to use if majority of the Compton ring is outside of the smaller FOV.

To illustrate the effects of these types of events, the forward projection of the Compton rings reconstructed for 4.44 MeV photons from an experimental PuBe source experiment, using CZT [shown in Fig. 4(b)], are separated as events resulting in a forward projection value greater than or equal to one, or approaching Limit 1, and events that result in a forward projection value less than one or those that approach Limit 2.

Fig. 1 displays 2-D histograms where each event is tallied for their non-zero pixels in the imaging frame and are separated based on their forward projection value which is calculated using (2), for both the 4π FOV and the 60° FOV imaging frame. This calculation is based on the first iteration where the initial image estimate is uniform that is

$$f_{j}^{n} = f_{j}^{0} = 1.$$

In the 4π FOV, the histograms in Fig. 1(a) and (b) show that all events result in a forward projection calculation of at least one or greater. Here, majority of the events are evenly distributed throughout the 4π FOV. The least amount of non-zero pixels are at the north and south poles of the image space,

which is expected, as the source is directly in front of the cathode side of the detector at (90°, 90°).

In comparison, the 60° FOV forward projection calculation shifts to values less than one for about 10% of the same events that were reconstructed in 4π. This is due to the truncation of the Compton rings in the smaller FOV. When focusing on only those events that have lower forward projection values, the histogram in Fig. 1(c) shows that majority of these events intersect pixels at the corners of the smaller imaging space. Whereas those events that have a forward projection of at least one or greater, shown in Fig. 1(d), have more Compton rings binned in the center pixels of the image space, where we expect to see the source distribution.

Realizing this phenomenon in a truncated FOV, we can then study the impact of events that result in low forward projection values on the portion of the LM-MLEM equation that provides the summed projection of all events in the image space

$$\sum_{i=1}^{I} \frac{t_{ij}}{\sum_{j'=1}^{J} t_{ij'} f_{j'}^{n}}. \tag{3}$$

Equation (3) can be interpreted as the back projection factor or the ratio of the system matrix elements of each event to its forward projection.

B. Back Projection Analysis

The backprojection factor of the first LM-MLEM iteration provides a first-order approximation of the photon distribution over the image space by summing the system matrix elements of all events divided by their respective forward projection, in each image pixel.

All subsequent iterations of (3) then provide a multiplicative correction to update the final image estimate. Fig. 2 shows the back projection factor calculated for the first five iterations in the 4π imaging space and in a 60° FOV for the same list-mode data shown in Fig. 1.

When comparing the back projection factor for the 4π FOV to the 60° FOV, the 4π FOV shows a hotspot for the estimated source distribution near (90°, 90°) and other Compton rings in the image space that are developing noise artifacts, but the 60° FOV results in very low values for majority of the inner pixels and amplified values in the corner pixels.

The intensity color bar for the 4π FOV shows that the highest intensity calculated by (3) for the backprojection factor of the first iteration is a value less than one, as expected since the initial image estimate is set to one for all pixels. However, the first iteration of the backprojection factor in the 60° FOV sharply increases to a very high value in the corners of the image space. The following iterations in the truncated FOV subsequently drop to lower intensity values as shown by the color bar, all attempts to reflect the more accurate estimation of the intensity of the source distribution.

Referring to Fig. 2(d), the line graph of the top row of pixels in the 60° FOV shows that for the first iteration's backprojection factor, the most intense pixels are at the corners, and the following iterations, begin to stabilize around a maximum intensity of one. However, the multiplicative correction of the source distribution in the subsequent backprojection factors
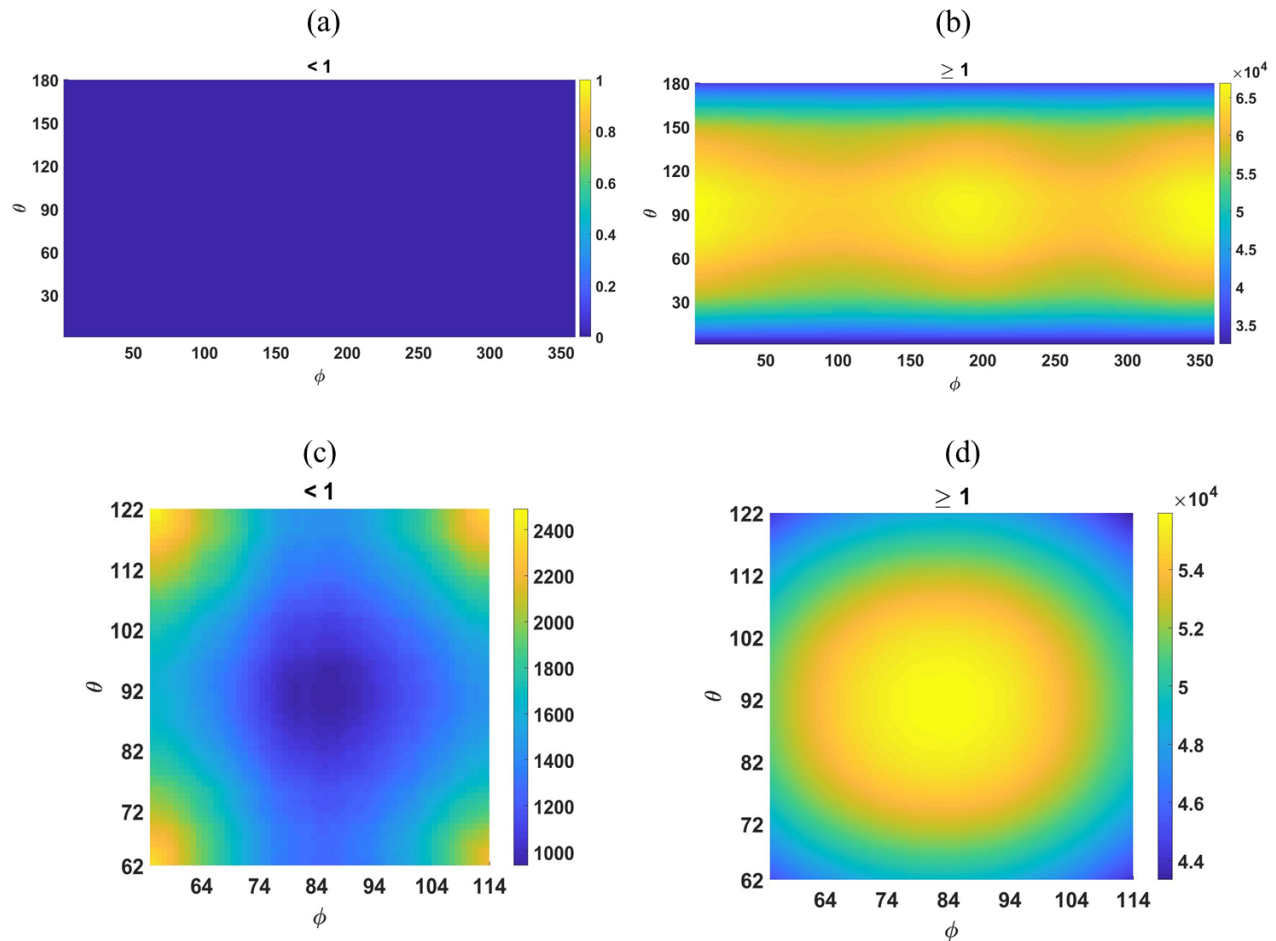
Fig. 1. 2-D histograms of the non-zero pixels of each Compton ring reconstructed in the 4π and 60° FOV, where the color bar represents the number of Compton rings binned for each pixel. (a) and (b) Correspond to all events in 4π with a forward projection value less than one and greater than or equal to one, respectively. (c) and (d) Correspond to all events that reconstruct within the 60° FOV with a forward projection value less than one and greater than or equal to one, respectively. The forward projection value for each event is calculated using (2).

will have no effect on the final image reconstruction, as it is dominated by the calculation of the first iteration.

Investigating the calculation of the backprojection factor in LM-MLEM reveals that the error in estimating the source distribution in a truncated space happens during the calculation of the first iteration. The calculation of the forward projection causes error in the truncated FOV likelihood estimate, particularly for events where majority of the Compton ring reconstructs outside the FOV. In truncated FOV imaging, Compton rings that are cropped by the smaller FOV will result in portions of the rings not being calculated as a part of the forward projection, and if heavily truncated can approach a very low likelihood estimate or Limit 2 as seen in Section II-A. This will result in high-intensity pixels for these types of events when calculating the back projection factor using (3). Fig. 1(c) shows that these events are most likely to occur near the corners of a smaller imaging space. Whereas those events with larger forward projection values, or approaching Limit 1, will most likely correspond to events that reconstruct well within the image space. However, the intensity of the backprojection factor of these events will lessen in their respective pixels, as the back projection factor of the LM MLEM equation is dividing each system

matrix element, t_{ij}, by a forward projection value greater than one.

For the example used in Fig. 1, when truncating the image space, only 10% of the events resulted in a forward projection value less than one, meaning that majority of the events reconstructed with a high forward projection and visually show to contribute the most to defining the expected source distribution in the 60° FOV as seen in Fig. 1(d). However, due to the calculation of the backprojection factor being a summation of a ratio, the 10% that approach Limit 2 are incorrectly amplified by this calculation for the first iteration which will translate to the final image reconstruction.

As the goal of the iterative process of LM-MLEM is to determine the most probable source distribution, the final image reconstruction will provide a maximized likelihood estimate of the source distribution reflected by the pixel intensity. When using LM-MLEM in a truncated FOV, back projecting those events with a high forward projection value will result in lower pixel values in the final image and will be visually overshadowed by those events with a low forward projection estimate. Events with low forward projection values are mostly reconstructing in the corner pixels due to be truncated by the smaller FOV but are amplified in the final image reconstruction
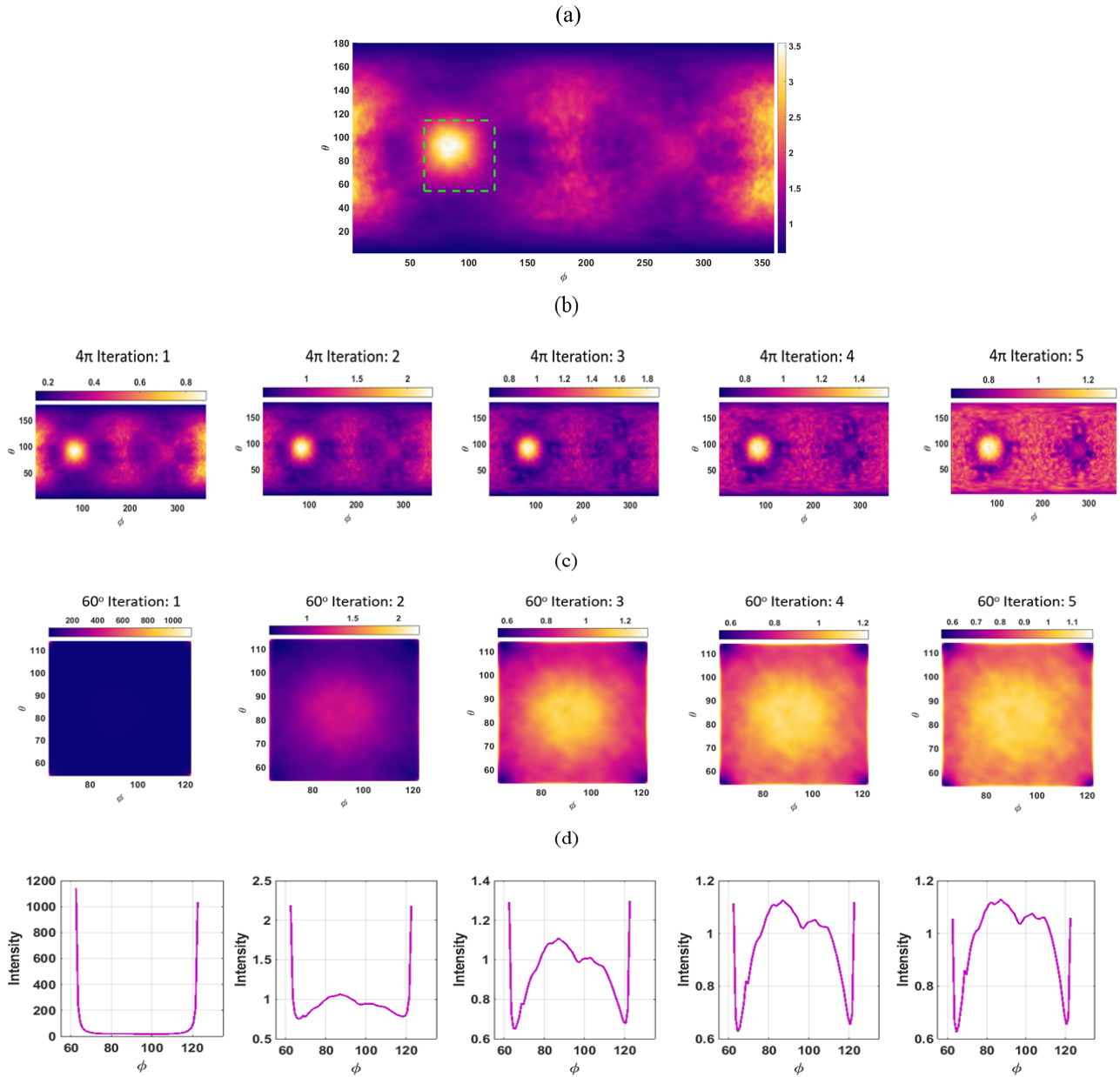
Fig. 2. (a) First iteration of a 4π MLEM image reconstruction of 4.44 MeV photons from experimental PuBe data. (b) 4π FOV backprojection factor calculated for the first five iterations in the 4π space, calculated using (3). (c) Back projection factors for the first five iterations calculated using (3), for a truncated $60°$ FOV of all Compton rings that intersect the FOV outlined by the dotted green line in (a). (d) Line plot of the intensity along the first row of the five backprojection factors shown in (c), highlighting the sharp corner convergence at $62°$ and $122°$.

in the first iteration of LM-MLEM due to their miscalculated backprojection factor. This pushes the MLEM equation to reconstruct a final image whose few pixels in the corner of the image space are seen as the most likely distribution of the source.

III. DERIVATION OF ROI-MLEM

Erroneous convergence to the amplified values at the corners of the image space when using LM-MLEM in a truncated FOV is in part due to the ill-weighted probability of each Compton ring that partially intersects the truncated FOV and produces an incorrectly amplified source distribution estimate in the image space. The algorithm needs to be revised to compensate for the full probability of each Compton ring regardless of its appearance in the ROI or truncated FOV. Thus, the proposed ROI-MLEM reconstruction method is designed based on the MLEM algorithm shown in (1).

To reframe the MLEM algorithm for a specified ROI smaller than the 4π imaging space, the system matrix for each event must be defined in two parts. One part defines the event probability (Compton ring) within the ROI and a second part that defines the same event in 4π, which will be denoted as the "background". The forward projection of the standard algorithm can then be broken into the summation of two components

$$\sum_{j'=1}^{J} t_{ij'} f_{j'}^{n} = B_i + \sum_{j'=1}^{J^R} t_{ij'}^{R} f_{j'}^{n,R}. \tag{4}$$
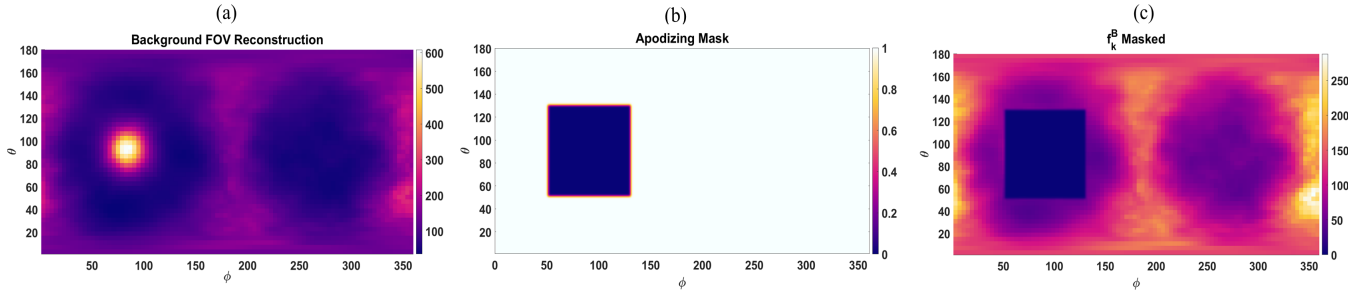
Fig. 3.   (a) First iteration of LM-MLEM of the background FOV which is multiplied by the (b) apodizing $\cos^2$ mask that smoothly transitions to the ROI where all pixel values go to zero in the (c) masked background projection.

This restructuring of the forward projection allows for the calculation of the source distribution within a smaller imaging space that sums all portions of the Compton ring probability: the portion within the ROI and the portion in the background. Here, $t_{ij'}^R$, defines the ROI system matrix elements, or the probability that the detected event originated from pixel j of the ROI space. The ROI can then be imaged using a fine pixel mesh grid, and now $j \in \{1, 2, \ldots, J^R\}$, where J^R is the total number of pixels defining the ROI space. Redefining the forward projection enables high spatial resolution imaging for the ROI alone.

The background is summed as a scalar constant for each photon event, B_i, and is expressed as

$$B_i = \sum_{k=1}^{K} \mathbf{f}_{k,\text{mask}}^B t_{ik}^B. \tag{5}$$

Equation (5) is the sum value of all background system matrix elements, t_{ik}^B which is the probability of each event, i, in each pixel, k, for a coarse mesh of K pixels in the 4π space, where $k \in \{1, 2, \ldots, K\}$. This is multiplied by $\mathbf{f}_{k,\text{mask}}^B$, which is the initial estimate of the background image space. The background projection, $\mathbf{f}_{k,\text{mask}}^B$, is the product of the first MLEM iteration, using (1), in the background FOV, by an apodizing mask. The mask is formed by convolving a uniform mask and a $\cos^2$ function that allows for a smooth transition to the ROI space in which the pixel values are zeroed, similar to Ziegler *et al.* [7]. Creating this mask ensures that the drastic change in the of the pixel values in the background and the zeroed ROI space does not create artifacts at the edges of the ROI. The mask also allows for the remaining probability values of each Compton ring outside of the ROI pixels to be included in the forward projection calculation in the ROI-MLEM equation. Without the addition of the background information, the corner convergence of MLEM will take place in our ROI.

Fig. 3 depicts the development of $\mathbf{f}_{k,\text{mask}}^B$ for the image reconstruction of a simulated gamma-ray point source. The background constant, B_i, is only calculated to provide the initial probability estimate of each Compton ring, ensuring that the full probability of each event in the 4π space is accounted for as we iterate over the smaller imaging space. The purpose of B_i is to suppress the ill-weighted Compton rings that intersect the ROI space in only the edge and corner pixels, these Compton rings would have resulted in low forward projection values without the addition of the
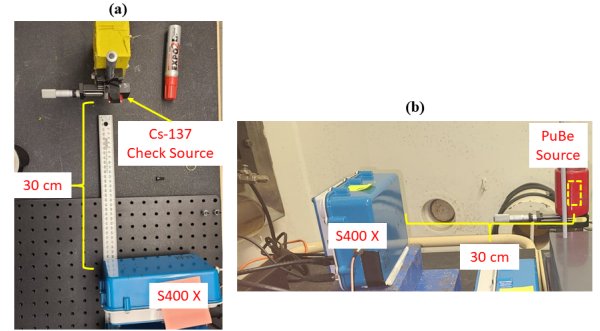

Fig. 4.   (a) ^{137}Cs experimental setup, the micrometer is used to shift the source from the "no shift" measurement location to the right by 3, 5, and 10 mm, each for 1-h measurements. (b) PuBe source experimental setup, the PuBe peg is an extended source approximately 2 in in length and 1 in diameter placed inside a small lead container 30 cm away from a S400X system. The source is shifted from left to right by 1 cm for two separate 3-h measurements.

background information. Whereas those events with high forward projection values, are shown to typically reconstruct well within the ROI space and will be associated with a low B_i constant as these Compton rings will intersect few pixels outside the ROI. And those events that reconstruct fully within the ROI space will have a B_i equal to zero and will remain unchanged in the ROI-MLEM update equation. The final form of the ROI-MLEM algorithm is

$$f_j^{n+1,R} = \frac{f_j^{n+1,R}}{s_j^R} \sum_{i=1}^{I} \frac{t_{ij}^R}{B_i + \sum_{j'=1}^{J^R} t_{ij'}^R f_{j'}^{n,R}} \tag{6}$$

where s_j^R, represents the sensitivity of the detector system to the photons emitted from all pixels in the ROI; for this work it is assumed to be uniform or equal to 1.

IV. APPLICATION OF ROI-MLEM

A. Near-Field Imaging Considerations

In far-field approximations, where the source is at such a distance from the detector that the imaging frame becomes much larger than the detector dimensions, the detector can be treated as a point detector. When doing so the vertex of all reconstructed Compton cones can be assumed to originate at the center of the detector system [11]. However, when the source is close to the detection system, or in the near-field, the detector size is no longer negligible and special consideration must be given to the positioning of each Compton cone.
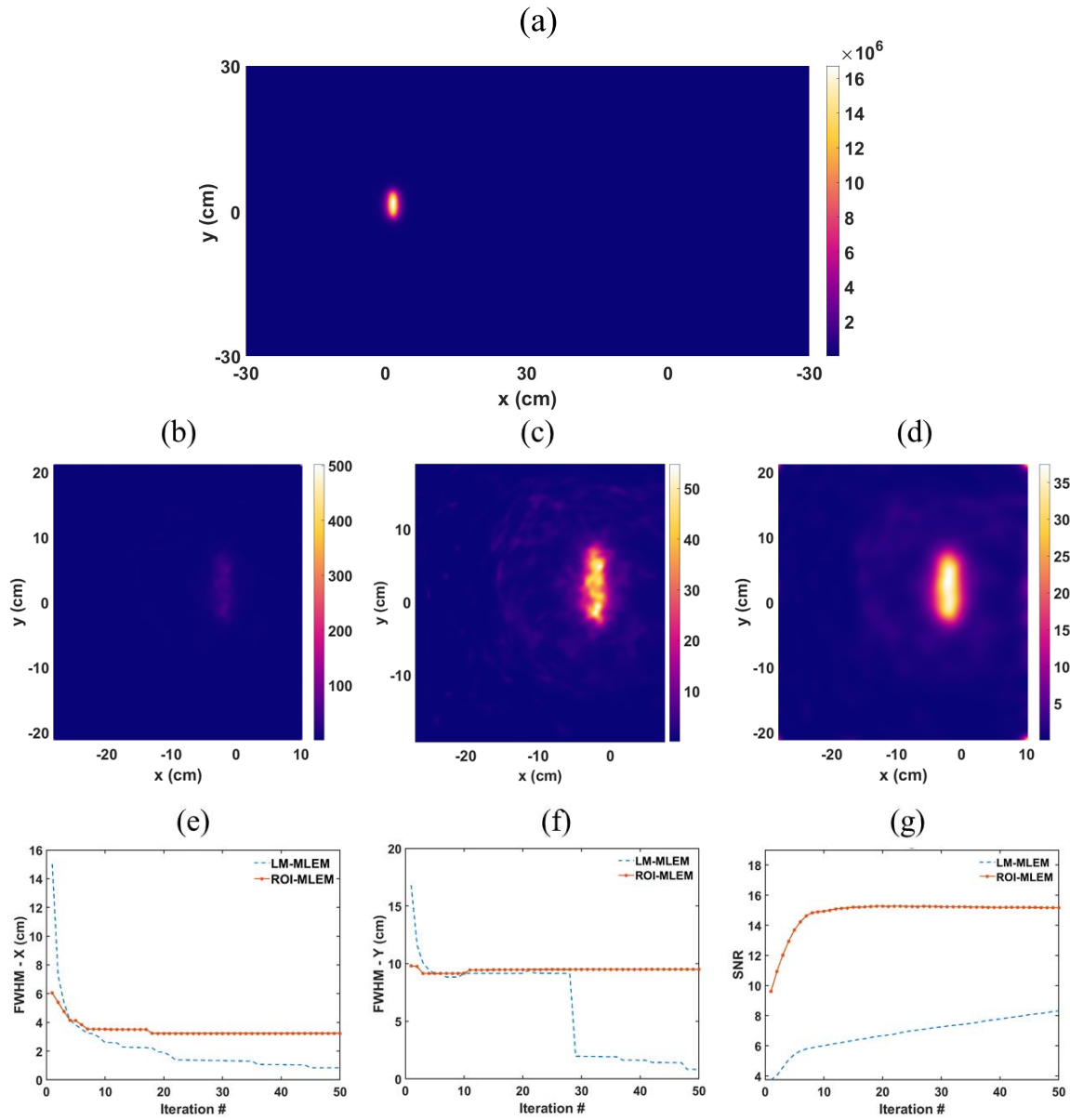
Fig. 5.   22nd iteration reconstructions of a simulated 10 cm ^{137}Cs line source in a (a) 4π LM-MLEM reconstruction, (b) LM-MLEM in a 90° FOV, (c) LM-MLEM 90° FOV with the outermost 10 edge pixels removed, and (d) ROI-MLEM reconstruction in a 90°. (e) and (f) Compares the FWHM values in the *x*- and *y*-directions, respectively, for both imaging algorithms, and (g) compares the SNR values for 50 iterations of both methods.

In the technique of near-field imaging, using 3-D position sensing CZT, the vertex location is corrected for by shifting it from the center of the detection system to the position of the first interaction of the photon event. When applying this correction, the radius of the imaging sphere must be preset such that the source is located correctly on the imaging sphere and the blur of the source distribution is properly compensated for.

B. Simulated and Experimental Datasets

We applied the iterative ROI-MLEM reconstruction algorithm to three sets of Compton imaging data gathered from list-mode gamma-ray events as follows.

1) A GEANT4 (version 4.10.02) simulation of a 10-cm ^{137}Cs line source with a 30 cm separation distance

between the source and a 2×2 array of CZT crystals that are 2.0 cm $\times$ 2.0 cm $\times$ 1.0 cm in dimension, with 0.5-cm spacing between each crystal. In the simulation, each crystal is capable of recording Compton scattering and full photoelectric absorption events per photon, with similar 3-D position sensitive accuracy (depth resolution of 0.5 mm), energy resolution (1% at 662 keV), providing the energy and x, y, and depth information of each interaction. 1E7 photons are emitted toward the detector from the line source and 40 000 photopeak events are used for image reconstruction.

2) Four experimental one-hour ^{137}Cs check source measurements were taken with a source to a detector distance of 30 cm away from a digital ASIC CZT system, the S400X^2 [16]. The CZT detection system, designed
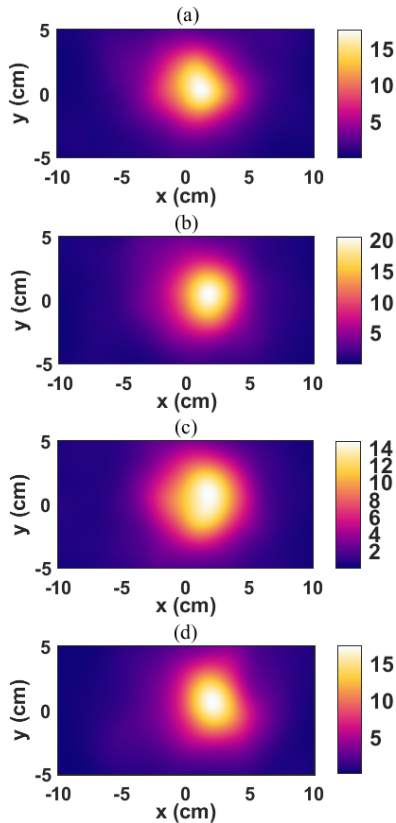
Fig. 6. ROI-MLEM reconstructions of the ^{137}Cs shifted source measurement. (a) No, (b) 3 mm, (c) 5 mm, and (d) 10 mm shift.

by H3D Inc., houses a 2 × 2 array of four CZT crystals that are 2.0 cm × 2.0 cm × 1.0 cm in dimension and have a 0.5 cm spacing between each crystal. The source is measured at a stationary position in front of the detector and then moved to the right by 3, 5, and 10 for three additional one-hour measurements, shown in Fig. 4(a).

3) Two 3-hour measurements were taken using a PuBe source at a 30 cm separation distance from a S400X system to detect and image the 4.44 MeV photon emitted from the alpha-Be interactions. The source was shifted by 1 cm to the right for the second measurement. The measurement setup is depicted by Fig. 4(b).

The simulated detection geometry and the CZT detection system both allow for Compton scattering events to be recorded independently for each crystal and co-dependently across the four crystals. All CZT crystals are equipped with a planar cathode, and a pixelated, 11 × 11, anode grid, allowing for 3-D interaction location estimation [17].

All ROI-MLEM image reconstructions shown are chosen based on the iteration with the max SNR value

$$\text{SNR} = \frac{P_{\text{signal}}}{P_{\text{noise}}} \tag{7}$$

where P_{signal}, is the summed value of all pixels in the image that correspond to a signal value of a least 50% of the max intensity of the image, normalized by the number of pixels that are at least 50% of the max intensity. P_{noise} is the standard

TABLE I
MLEM ALGORITHM RECONSTRUCTION COMPARISON

Method	SNR	FWHM-X (± 0.28 cm)	FWHM-Y (± 0.28 cm)
LM-MLEM	6.77	1.40 cm	9.17 cm
ROI-MLEM	15.28	3.24 cm	9.49 cm

Comparison of the SNR and FWMH of the image reconstructions developed using LM-MLEM and ROI-MLEM of the 10 cm ^{137}Cs line source simulation. The FWHM error is taken as twice the pixel pitch.

deviation of all remaining pixels in the image that have a value less than 50% than the max intensity of the image.

To compare standard MLEM SNR to the ROI-MLEM SNR the signal pixels are chosen from the inner most pixels of the image excluding the outer edge pixels. This alleviates the signal being read as only the corners and allows for evaluation of the source distribution calculated by MLEM.

V. IMAGING RESULTS

A. Simulated 10 cm ^{137}Cs Line Source

For proof of concept, image reconstructions of a simulated 10 cm ^{137}Cs line source are compared using both MLEM and ROI-MLEM in a 90° FOV. Using the 662 keV energy line ensures a noise-less simulated dataset for CZT detection, which should favor the image reconstruction using both ROI-MLEM and standard MLEM. Both reconstruction methods used 40 000 photopeak events in an energy window of 657 to 667 keV and utilized 300 × 300 pixels for a pixel resolution of 0.3°. Fig. 5 shows the image reconstruction for the 22nd iteration of both the ROI-MLEM and MLEM method based on the max SNR value given by the ROI-MLEM method as the MLEM method resulted in a rising slope of the SNR calculation as a function of iteration also shown in Fig. 5.

The image reconstructions show that the ROI-MLEM algorithm results in a clearer and more uniform representation of the simulated line source. At the same iteration, MLEM starts to break apart the source distribution, causing noise artifacts that deviate from a single uniform source distribution, which could be due to the altered convergence rate of MLEM in the truncated space, which focuses on the amplified corners. The full 4π reconstruction shown in Fig. 5(a) shows that the source distribution is more comparable to that of the ROI-MLEM reconstruction.

Table I indicates the FWHM values in both directions taken through the peak centroid of each image reconstruction and the SNR value for the 22nd iteration shown in Fig. 5. ROI-MLEM results in a closer estimate of the sources true length but a wider estimate in the x-direction of its width. This could be due to the inherent Gaussian uncertainty of the Compton rings in the near-field [11], and ROI-MLEM enhancing those rings that converge within the ROI and not near the edges. Although the MLEM reconstruction results in a thinner line source it suffers from a poorer uniformity in the sources intensity which also affects the fit applied to the FWHM calculation.
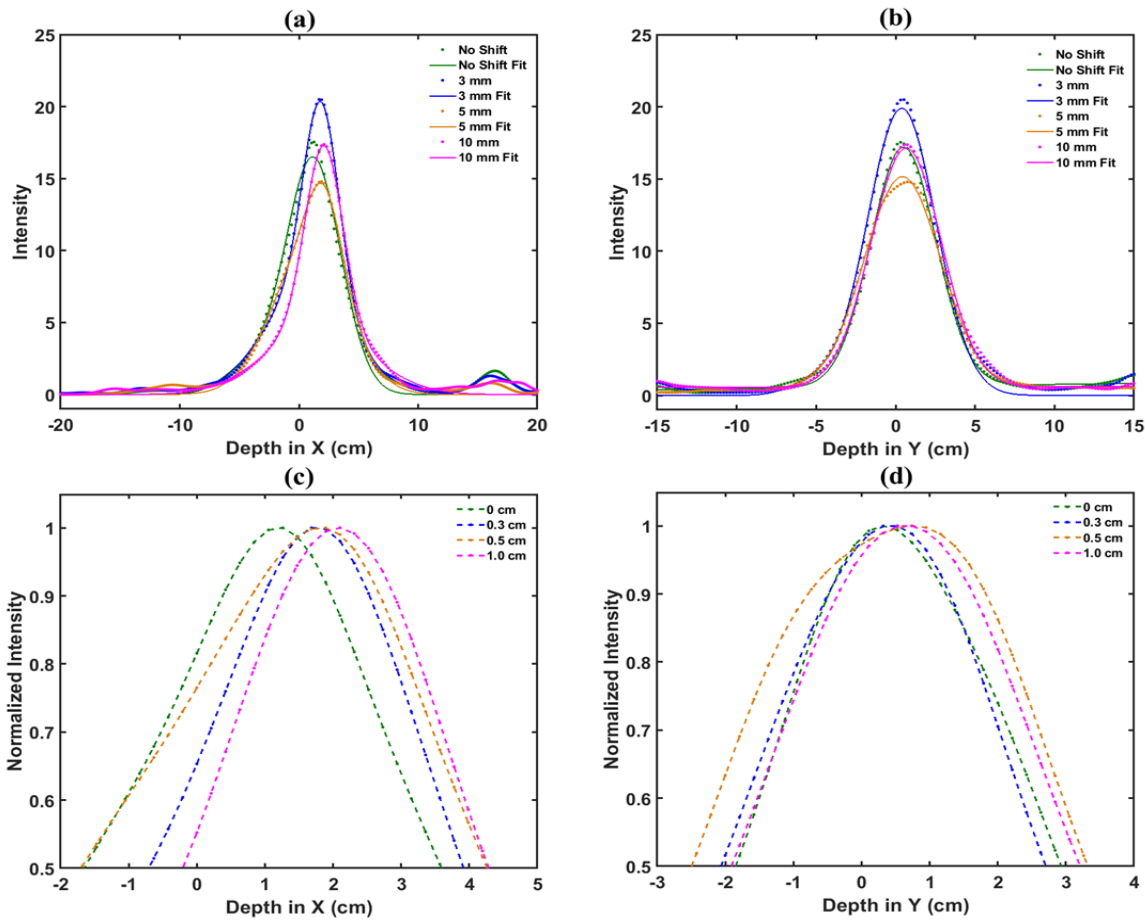
Fig. 7. 1-D profiles through and Gaussian fit of the peak centroids in the (a) *x*- and (b) *y*-directions for the image reconstructions shown for the ^{137}Cs shifted source measurement. (c) and (d) Top 50% of the intensity normalized by the peak value in the *x*- and *y*-directions, respectively.

B. ^{137}Cs Shifted Source Measurement

To demonstrate the high-resolution capabilities of ROI-MLEM for imaging analysis, the optimal ROI-MLEM iteration reconstructions, based on the SNR value, are shown for each measured position of the ^{137}Cs source in Fig. 6. Iterations 25, 25, 26, and 27 resulted in the max SNR iteration for the "No Shift," "3," "5," and "10 mm" reconstructions, respectively. The ROI is designed as a rectangular frame spanning 60° in the polar and 90° in the azimuthal, utilizing 300 × 450 pixels resulting in a 0.2° pixel resolution. The images are cropped along the x-direction in Fig. 6 to focus on the shift of the source from left to right. The reconstructions show that the position resolution is not fine enough to separate the sources if they were reconstructed in the same image, as the average FWHM in the *x*-direction (left to right) for each measurement is 4.93 ± 0.40 cm. The FWHM of each source reconstruction is much larger than the shift increments as seen in Fig. 7(c). However, comparing the 1-D profile through the peak centroid of the source distribution shows that the source's location can be estimated from the peak centroid values in Table II, derived from Fig. 7. For each profile, a Gaussian fit is applied and the peak location of both the data and the fit are compared. The average error based on the three shifted source locations is 1.7 and 1.4 mm for the Gaussian fit and 1-D profiles, respectively. Table II shows

TABLE II
PEAK CENTROID LOCATION ESTIMATION

Shift	Peak Location (mm)		Difference (mm)	
	Fit ($\overline{RMSE}$=0.19)	Data (±0.20)	Fit	Data
No Shift	11.5	12.6	--	--
3 mm	17.3	16.8	5.8	4.2
5 mm	18.2	18.9	6.7	6.3
10 mm	21.0	21.0	9.5	8.4

Source distribution location estimation based on the peak centroid location in the x-direction of the 1D profiles of the image reconstructions shown in Fig. 6 and Fig. 7.

that the largest error in the shift estimation comes from the fit's location estimate which could be due to the spread in the source distribution.

C. PuBe Source Experiment

To examine the performance of ROI-MLEM for high energy gamma-ray imaging, the 4.44-MeV photopeak emitted from alpha interactions with beryllium in a PuBe source was reconstructed for each 3-h measurement, one of which is used for the example shown in Fig. 1 (left measurement in Fig. 8). 25 000 4.44 MeV photopeak events are used for ROI-MLEM image reconstructions in 90° FOV with a pixel
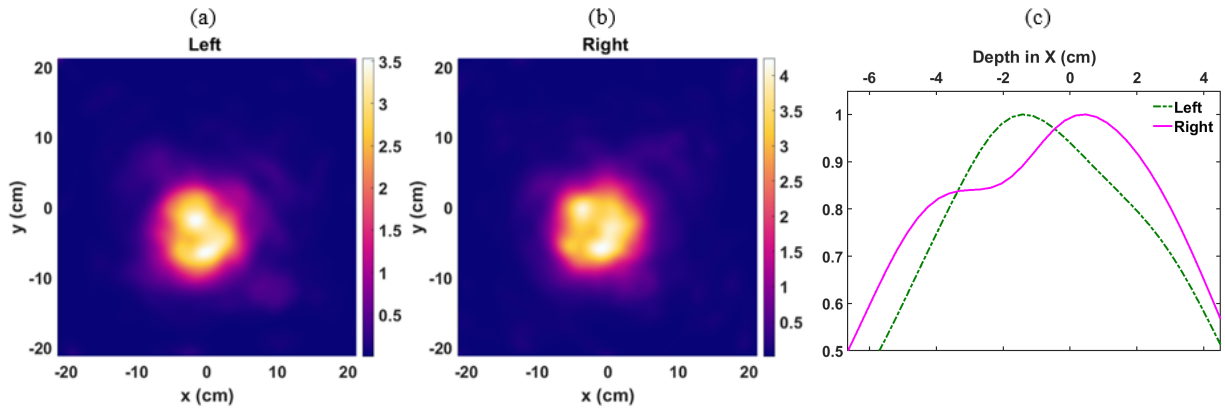
Fig. 8. 25th iteration of ROI-MLEM reconstructions of the 4.44 MeV photopeak from two PuBe source measurements. The source was shifted from (a) left to (b) right by 1 cm for 3-h measurements. (c) 1-D profile through the peak centroid along the x-axis shows the shift in the max intensity between each source distribution reconstruction.

TABLE III
TIME TO RECONSTRUCT THE FIRST ITERATION COMPARISON

	# Of Pixels ($\Phi \times \theta$)	Pixel Res.	Time (s)	RAM Usage‡
MLEM 4π	720×360	0.5º	338	41.3%
MLEM 60º	120×120	0.5º	21	10.0%
MLEM 90º	300×300	0.3º	116	11.1%
ROI-MLEM 90º	300×300	0.3º	132	11.7%

20,000 4.44 MeV photopeak events reconstructed for the first iteration of standard list-mode MLEM and ROI-MLEM.

‡ Calculated as the average storage use from 126 GB of available memory.

resolution of 0.3°. Fig. 8 illustrates the image reconstructions of both measurements. At this high photopeak energy, CZT suffers in a worsened energy resolution which broadens the photopeak, resulting from many partial energy deposition events and poorly reconstructed events due to charge sharing, which translates to the imaging space [15]. For these reconstructions, a broad energy window of 100 keV, about the photopeak, was used to collect statistically enough events for imaging. Although, the images show a bright hotspot with little noise interference (in comparison to the 4π projection shown in Fig. 1) the source distribution is much larger than the size of the original source. Averaging the FWHM for both reconstructions, the source distribution measures 9.45 ± 0.05 cm $\times$ 11.27 ± 0.05 cm in the x- and y-directions, respectively. The spread and irregularity in the hotspot could be due to the extent of the PuBe peg from its cylindrical shape and the poorer statistics under such a broad photopeak coupled with the complications with Compton imaging high-energy photopeaks detected by CZT. Fig. 8(c) shows a 1-D profile along the x-direction through the location of the most intense spot or peak centroid of each image reconstruction. When comparing the peaks of both profiles, we estimate a shift of 0.93 ± 0.1 cm.

D. Computational Performance

Table III reflects the reduction in computational expense when reconstructing the 4.44 MeV photopeak events using

ROI-MLEM. We compare the time to reconstruct the first iteration as this step includes the calculation of the system matrix as well. The time to reconstruct the first iteration is reduced by 61% when comparing a 4π reconstruction to the ROI-MLEM reconstruction of the same number of events. The 4π image reconstruction pixel resolution is limited by the computational constraints of the computing system used for this work, however, is comparable to the resolution of the other tested imaging frames. When comparing the same 90° FOV reconstructions using standard MLEM and ROI-MEM, the timing and computational use differs slightly, ROI-MLEM being greater due to the computation used for the background system matrix constants, which is only computed once, and the values are stored for use in the following iterations. The background constant, used for the images shown in Fig. 8, is calculated using a 4° pixel resolution (4050 pixels over a 4π space). This calculation can be optimized for each imaging problem, based on resolution requirements, and improving accuracy of estimating the Compton ring, adding little expense in the computation of the first iteration.

VI. CONCLUSION

This article demonstrates the use of a novel ROI-MLEM algorithm to effectively Compton image sources in a truncated image space. By truncating the imaging space to a specified region, the image spatial resolution can be enhanced by utilizing an optimized number of pixels for just the ROI itself. ROI-MLEM corrects for the inherent convergence of MLEM to the corners of the ROI imaging space by considering the contribution of each event to both the 4π space and the ROI. Using standard MLEM, in a ROI smaller than 4π, these corners would converge with a greater intensity than the true source distribution, which would make it difficult to use for further analysis.

Applying this method to a simulated line source shows that the source reconstruction can be enhanced well enough to provide an estimate of the source shape and extent with an absolute error of 5.1%. This method also shows its use in estimating source location with submillimeter pixel resolution, from experimental data using a ^{137}Cs check source, resulting in an average 1.7 mm error when applying a Gaussian fit. Studies of the ROI-MLEM algorithm's use in high-energy photon

imaging shows the capability of the algorithm to estimate a high-energy extended source shift in space within good agreement of the true shift of the source. The computational performance of ROI-MLEM shows capability of reducing the time to reconstruct an image by nearly a third of the time using standard MLEM in a 4π space with comparable resolution.

Further work will be done to investigate the use of the ROI-MLEM algorithm impact on prompt gamma-ray imaging for proton beam range verification where the chance of high-frequency noise and image artifacts are increased. The application of ROI-MLEM could also be extended to 3-D applications, using CZT systems as 3-D reconstructions can be ascertained provided the event reconstruction of each Compton ring. This can allow for a third dimension of depth information in the imaging space, while enhancing computational performance when imaging an extended source in the near-field of the detection system. There is also room for improvement on the Gaussian uncertainty associated with each Compton ring reconstructed in the ROI for near-field imaging applications.

REFERENCES

[1] J. C. Polf, S. Avery, D. S. Mackin, and S. Beddar, "Imaging of prompt gamma rays emitted during delivery of clinical proton beams with a Compton camera: Feasibility studies for range verification," *Phys. Med. Biol.*, vol. 60, no. 18, pp. 7085–7099, Sep. 2015.

[2] P. Solevi *et al.*, "Performance of MACACO Compton telescope for ion-beam therapy monitoring: First test with proton beams," *Phys. Med. Biol.*, vol. 61, no. 4, 2016, Art. no. 5149.

[3] A. Sen, D. Labate, B. Bodmann, and R. Azencott, "3D ROI image reconstruction from truncated computed tomography," *IEEE Trans. Med. Imag.*, vol. 11, no. 9, pp. 1–19, 2013.

[4] E. Y. Sidky, D. N. Kraemer, E. G. Roth, C. Ullberg, I. S. Reiser, and X. Pan, "Analysis of iterative region-of-interest image reconstruction for X-ray computed tomography," *J. Med. Imag.*, vol. 1, no. 3, Oct. 2014, Art. no. 031007.

[5] B. Zhang and G. L. Zeng, "Two-dimensional iterative region-of-interest (ROI) reconstruction from truncated projection data," *Med. Phys.*, vol. 34, no. 3, pp. 935–944, Feb. 2007.

[6] Y. Zhang, J. A. Fessler, N. H. Clinthorne, and W. L. Rogers, "A hybrid-grid parameterization method for SPECT reconstruction," *J. Nucl. Med.*, vol. 36, no. 4, p. 172, 1995.

[7] A. Ziegler, T. Nielsen, and M. Grass, "Iterative reconstruction of a region of interest for transmission tomography," *Med. Phys.*, vol. 35, no. 4, pp. 1317–1327, Mar. 2008.

[8] C. E. Lehner, Z. He, and F. Zhang, "4π Compton imaging using a 3-D position-sensitive CdZnTe detector via weighted list-mode maximum likelihood," in *Proc. IEEE Nucl. Sci. Symp. Conf. Rec.*, vol. 5, Oct. 2003, pp. 3691–3694.

[9] S. J. Wilderman, N. H. Clinthorne, J. A. Fessler, and W. L. Rogers, "List-mode maximum likelihood reconstruction of Compton scatter camera images in nuclear medicine," in *Proc. IEEE Nucl. Sci. Symp. Med. Imag. Conf.*, vol. 3, Nov. 1999, pp. 1716–1720.

[10] M. Sakai, Y. Kubota, R. K. Parajuli, M. Kikuchi, K. Arakawa, and T. Nakano, "Compton imaging with ^{99m}Tc for human imaging," *Sci. Rep.*, vol. 9, no. 1, Dec. 2019, Art. no. 12906.

[11] D. Xu, Z. He, C. E. Lehner, and F. Zhang, "4-pi Compton imaging with single 3D position-sensitive CdZnTe detector," *Proc. SPIE*, vol. 5540, pp. 144–155, Oct. 2004.

[12] J. Chu, "Advanced imaging algorithms with position-sensitive gamma-ray detectors," Ph.D. dissertation, Dept. Nucl. Eng. Radiological Sci., Univ. Michigan, Ann Arbor, MI, USA, 2018.

[13] D. Goodman, J. Xia, and Z. He, "Qualitative measurement of spatial shielding isotopics via Compton imaging neutron-induced gamma rays using 3-D CdZnTe detectors," *Nucl. Instrum. Meth. Phys. Res. A, Accel. Spectrom. Detect. Assoc. Equip.*, vol. 935, pp. 214–221, Aug. 2019.

[14] W. Wang, W. R. Kaye, J. C. Kim, F. Zhang, and Z. He, "Improvement of Compton imaging efficiency by using side-neighbor events," *Nucl. Instrum. Meth. Phys. Res. A, Accel. Spectrom. Detect. Assoc. Equip.*, vol. 687, pp. 62–68, Sep. 2012.

[15] D. Shy, J. Xia, and Z. He, "Artifacts in high-energy Compton imaging with 3-D position-sensitive CdZnTe," *IEEE Trans. Nucl. Sci.*, vol. 67, no. 8, pp. 1920–1928, Aug. 2020.

[16] F. Zhang, C. Herman, Z. He, G. De Geronimo, E. Vernon, and J. Fried, "Characterization of the H3D ASIC readout system and 6.0 cm^3 3-D position sensitive CdZnTe detectors," *IEEE Trans. Nucl. Sci.*, vol. 59, no. 1, pp. 236–242, Feb. 2012.

[17] Z. He, W. Li, G. F. Knoll, D. K. Wehe, J. Berry, and C. M. Stahle, "3-D position sensitive CdZnTe gamma-ray spectrometers," *Nucl. Instrum. Meth. Phys. Res. A, Accel. Spectrom. Detect. Assoc. Equip.*, vol. 422, nos. 1–3, pp. 173–178, 1999.